Draft version February 15, 2022
Typeset using LaTeX twocolumn style in AASTeX631

Schwarzschild and Ledoux are equivalent on evolutionary timescales

Evan H. Anders,[1,2] Adam S. Jermyn,[3,2] Daniel Lecoanet,[1,4,2] Adrian E. Fraser,[5,2] Imogen G. Cresswell,[6,2] and J. R. Fuentes[7]

[1]*CIERA, Northwestern University, Evanston IL 60201, USA*
[2]*Kavli Institute for Theoretical Physics, University of California, Santa Barbara, CA 93106, USA*
[3]*Center for Computational Astrophysics, Flatiron Institute, New York, NY 10010, USA*
[4]*Department of Engineering Sciences and Applied Mathematics, Northwestern University, Evanston IL 60208, USA*
[5]*Department of Applied Mathematics, Baskin School of Engineering, University of California, Santa Cruz, Santa Cruz, CA 95064, USA*
[6]*Department Astrophysical and Planetary Sciences & LASP, University of Colorado, Boulder, CO 80309, USA*
[7]*Department of Physics and McGill Space Institute, McGill University, 3600 rue University, Montreal, QC H3A 2T8, Canada*

(Received; Revised; Accepted; Published)

Submitted to ApJ

ABSTRACT

In one-dimensional stellar evolution models, convective boundaries are calculated using either the Schwarzschild or Ledoux criterion, but there is no consensus regarding which criterion to use. In this letter, we present a 3D hydrodynamical simulation of a convection zone and adjacent radiative zone, including both thermal and compositional buoyancy forces. Turbulent convection only occurs in the region which is unstable according to the Ledoux criterion. Early in the simulation, the stable region adjacent to the convection zone is Schwarzschild unstable but Ledoux stable, due to a composition gradient. Over many convective overturn timescales the convection zone grows via entrainment. The convection zone saturates at the size predicted by the Schwarzschild criterion, and in this final state the Schwarzschild and Ledoux criteria are equivalent. Therefore, the size of stellar convection zones is determined by the Schwarzschild criterion, except possibly during short-lived stages in which entrainment persists.

Keywords: Stellar convection zones (301), Stellar physics (1621); Stellar evolutionary models (2046)

1. INTRODUCTION

We do not understand convective boundaries in stars. This is suggested by a variety of observations; for example, models and observations disagree about the sizes of convective cores (Claret & Torres 2018; Viani & Basu 2020; Pedersen et al. 2021; Johnston 2021), lithium abundances in solar-type stars (Pinsonneault 1997; Sestito & Randich 2005; Carlos et al. 2019; Dumont et al. 2021), and the sound speed at the base of the Sun's convection zone (see Basu 2016, Sec. 7.2.1). Improperly estimating convective boundary locations can have important impacts across astrophysics such as affecting the mass of stellar remnants (Farmer et al. 2019; Mehta et al. 2022) and the inferred radii of exoplanets (Basu et al. 2012; Morrell 2020).

While convective boundary mixing (CBM) has many uncertainties, the most fundamental question is: what determines the location of convection zone boundaries? Some stellar evolution models determine the location of the convection zone boundary using the *Schwarzschild criterion*, by comparing the radiative and adiabatic temperature gradients. In other models, the convection zone boundary is determined by using the *Ledoux criterion*, which also accounts for compositional stratification (Salaris & Cassisi 2017, chapter 3, reviews these criteria). Recent work states that these criteria should be equivalent at a convective boundary according to mixing length theory (Gabriel et al. 2014; Paxton et al. 2018, 2019), but in practice these criteria are often different at convective boundaries in stellar evolution software in-

Corresponding author: Evan H. Anders
evan.anders@northwestern.edu

struments, and this has led to a variety of workarounds (Paxton et al. 2018, 2019).

As there is still disagreement regarding which stability criterion is appropriate for 1D modeling (see Kaiser et al. 2020, chapter 2), insight can be gained from studying multi-dimensional simulations. Such simulations show that convection zones adjacent to a Ledoux stable region can expand by entraining material from the stable region (Meakin & Arnett 2007; Woodward et al. 2015; Jones et al. 2017; Cristini et al. 2019; Fuentes & Cumming 2020; Andrassy et al. 2020, 2021). However, past simulations have not achieved a statistically-stationary state, leading to uncertainty in how to include entrainment in 1D models (Staritsin 2013; Scott et al. 2021).

In this letter, we present a 3D hydrodynamical simulation that demonstrates that convection zones adjacent to regions that are Ledoux-stable but Schwarzschild unstable will entrain material until the adjacent region is stable by both criteria. Therefore, in 1D stellar evolution models, the Schwarzschild criterion correctly determines the location of the convective boundary when evolutionary timescales are much larger than the convective overturn timescale (e.g., on the main sequence; Georgy et al. 2021). When correctly implemented, the Ledoux criterion should return the same result (Gabriel et al. 2014). We discuss these criteria in Sec. 2, describe our simulation in Sec. 3, and briefly discuss the implications of our results for 1D stellar evolution models in Sec. 4.

2. THEORY & EXPERIMENT

Convective stability can be determined using the Schwarzschild criterion,

$$\mathcal{Y}_{\rm S} \equiv \nabla_{\rm rad} - \nabla_{\rm ad}, \tag{1}$$

or the Ledoux criterion,

$$\mathcal{Y}_{\rm L} \equiv \mathcal{Y}_{\rm S} + \frac{\chi_\mu}{\chi_T}\nabla_\mu. \tag{2}$$

The temperature gradient $\nabla \equiv d\ln P/d\ln T$ (pressure P and temperature T) is $\nabla_{\rm ad}$ for an adiabatic stratification and $\nabla_{\rm rad}$ if the flux is entirely carried radiatively. The composition gradient $\nabla_\mu = d\ln\mu/d\ln P$ (mean molecular weight μ) is modified by $\chi_T = (d\ln P/d\ln T)_{\rho,\mu}$ and $\chi_\mu = (d\ln P/d\ln\mu)_{\rho,T}$ (density ρ).

In Eqns. 1 and 2, $\mathcal{Y}$ is the discriminant (e.g., Paxton et al. 2018, sec. 2), which is like the superadiabaticity. Stellar structure software instruments assume that convective boundaries coincide with the root (sign change) of the discriminant. The various stability regimes which can occur in stars are described in section 3 and figure 3 of Salaris & Cassisi (2017), but note four important regimes:

1. Convection Zones (CZs): Regions with both $\mathcal{Y}_{\rm S} > 0$ and $\mathcal{Y}_{\rm L} > 0$ are convectively unstable.
2. Radiative Zones (RZs): Regions with $\mathcal{Y}_{\rm S} < 0$ and $\mathcal{Y}_{\rm L} \leq \mathcal{Y}_{\rm S}$ are stable to convection.
3. "Semiconvection" Zones (SZs): Regions with $\mathcal{Y}_{\rm S} > 0$ but $\mathcal{Y}_{\rm L} < 0$ are stablized to convection by a composition gradient despite an unstable thermal stratification. These regions can be stable RZs or linearly unstable to oscillatory double-diffusive convection (ODDC, see Garaud 2018, chapters 2 and 4).
4. "Thermohaline" Zones: Regions with $\mathcal{Y}_{\rm S} < 0$ and $\mathcal{Y}_{\rm L} > \mathcal{Y}_{\rm S}$ are thermally stable to convection despite an unstable composition gradient. These regions can be stable RZs or linearly unstable to thermohaline mixing (see Garaud 2018, chapters 2 and 3).

In this letter, we study 3D simulations of a stable SZ (#3) bounded below by a CZ (#1) and above by an RZ (#2). We examine how the boundary of the CZ evolves through entrainment. In particular, we are interested in seeing if the roots of $\mathcal{Y}_{\rm S}$ and $\mathcal{Y}_{\rm L}$ coincide on timescales that are long compared to the dynamical timescale but short compared to evolutionary timescales.

In this work, we utilize a simplified 3D model employing the Boussinesq approximation, which assumes that the depth of the layer being studied is much smaller than the local scale height. We study a domain consisting of a thin (much smaller than a scale height) region near a convective boundary, so this assumption is valid. The relevant physics for this problem are included ($\nabla_{\rm rad}$ varies with height, buoyancy is determined both by the composition μ and the temperature stratification T), so $\mathcal{Y}_{\rm S}$ and $\mathcal{Y}_{\rm L}$ are meaningfuly defined and distinct from one another when composition gradients are present. For details on our model setup and Dedalus simulations, we refer the reader to appendices A and B.

3. RESULTS

Fig. 1 visualizes the composition field in our simulation near the initial state (left) and evolved state (right). Overplotted horizontal lines correspond to the roots of $\mathcal{Y}_{\rm L}$ (orange, Ledoux boundary) and $\mathcal{Y}_{\rm S}$ (purple, Schwarzschild boundary). Initially, the bottom third of the domain is a CZ, the middle third is an SZ, and the top third is an RZ. Convection mechanically overshoots at all times, which can be seen by the presence of convection slightly above the orange Ledoux boundary. Overshoot occurs because the Ledoux boundary is not the location where convective velocity is zero, but rather the

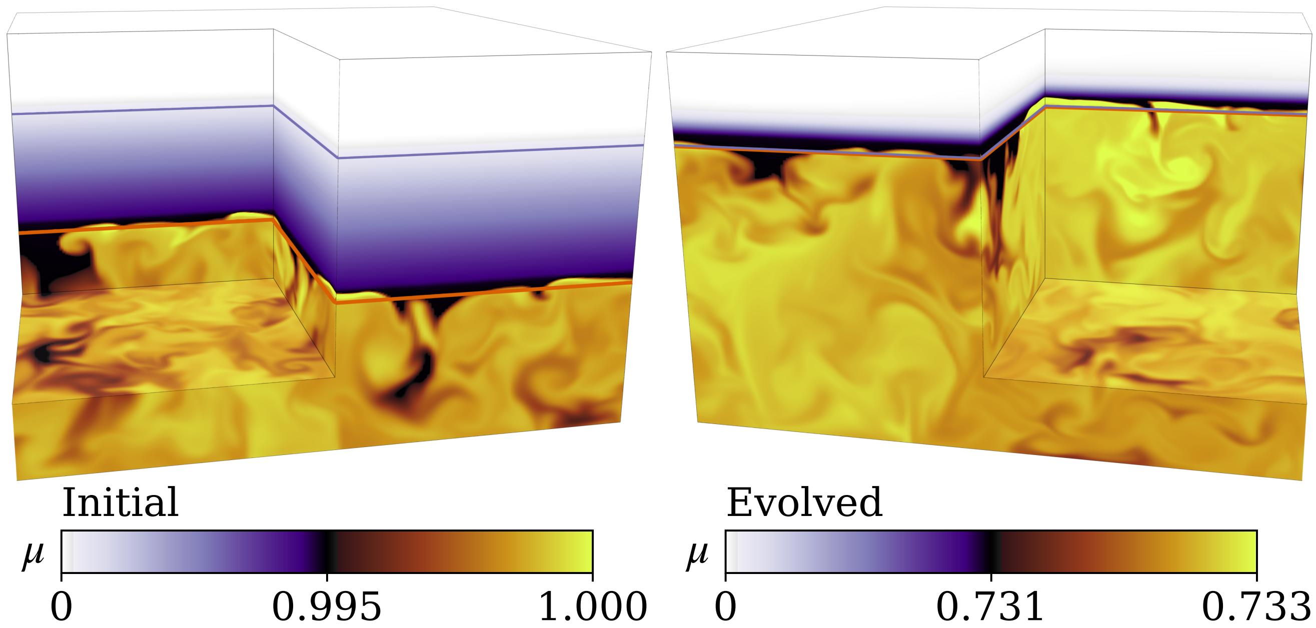

Figure 1. Volume renderings of the simulation composition field μ at early (left) and late (right) times. The change in color from white at the top of the box to dark purple at the top of the convection zone denotes a stable composition gradient. The convection zone is mostly well-mixed, so we expand the colorbar scaling there; black represents entrained low-μ fluid being mixed into the yellow high-μ convection zone. The orange and purple horizontal lines respectively denote the Ledoux and Schwarzschild boundaries. The simulation domain spans $z = [0, 3]$, but we only plot $z = [0, 2.5]$ here.

location where buoyant acceleration changes sign due to a sign change in the entropy gradient.

The most obvious change from the left to the right panel is that the CZ has consumed the SZ and fills the bottom two-thirds of the box. The overshooting convective motions entrained low-composition material from above the Ledoux boundary into the CZ. Convective motions mixed this fluid, and this process repeated over thousands of convective overturn times until the Ledoux and Schwarzschild boundaries of the CZ coincided. After becoming Schwarzschild stable, the convective boundary stopped moving. This occurs because the radiative flux renews and reinforces the radiative gradient, but there is no equivalent process for the composition[1].

Figure 2 displays vertical simulation profiles in the initial (left) and evolved (right) states. Shown are the composition μ (top), the discriminants $\mathcal{Y}_\mathrm{L}$ and $\mathcal{Y}_\mathrm{S}$ (middle), and the square Brunt-Väisälä frequency (top) as well as the square convective frequency defined as

$$f_\mathrm{conv}^2 = \frac{|\boldsymbol{u}|^2}{\ell_\mathrm{conv}^2}, \tag{3}$$

where $|\boldsymbol{u}|$ is the horizontally-averaged velocity magnitude and ℓ_conv is the depth of the convectively unstable layer.

Initially, the composition is uniform in the CZ ($z < 1$) and RZ ($z > 2$), but varies linearly in the SZ ($z \in [1, 2]$). The root of $\mathcal{Y}_\mathrm{L}$ occurs at $z \approx 1$ while that of $\mathcal{Y}_\mathrm{S}$ occurs at $z \approx 2$. Furthermore, $f_\mathrm{conv}^2 = 0$ in the initial, stationary state. The Brunt-Väisälä frequency N^2 is negative in a boundary layer at the base of the CZ which drives the instability. N^2 is stable for $z \gtrsim 1$, and is larger in the RZ than the SZ by an order of magnitude[2]

The evolved state is attained after convection entrains and mixes the stabilizing fluid in the SZ. We see that the composition profile (top) is constant in the CZ and overshoot zone (denoted as a transparent hashed region), but approximates a step function at the top of the overshoot zone. The roots of the discriminants $\mathcal{Y}_\mathrm{L}$ and $\mathcal{Y}_\mathrm{S}$ coincide (middle). Furthermore, in the CZ, the convective frequency is roughly constant and $N^2 \lesssim 0$ (bottom). In the RZ, $f_\mathrm{conv}^2 \approx 0$ and $N^2 \gg 0$. We can compute the

[1] Nuclear timescales are generally much longer than dynamical timescales and can be neglected as a source of composition.

[2] We ran simulations where N^2 was identical in the RZ and SZ and saw similar behavior. We make N^2 large in the RZ to reduce overshoot and wave mixing in the evolved state.

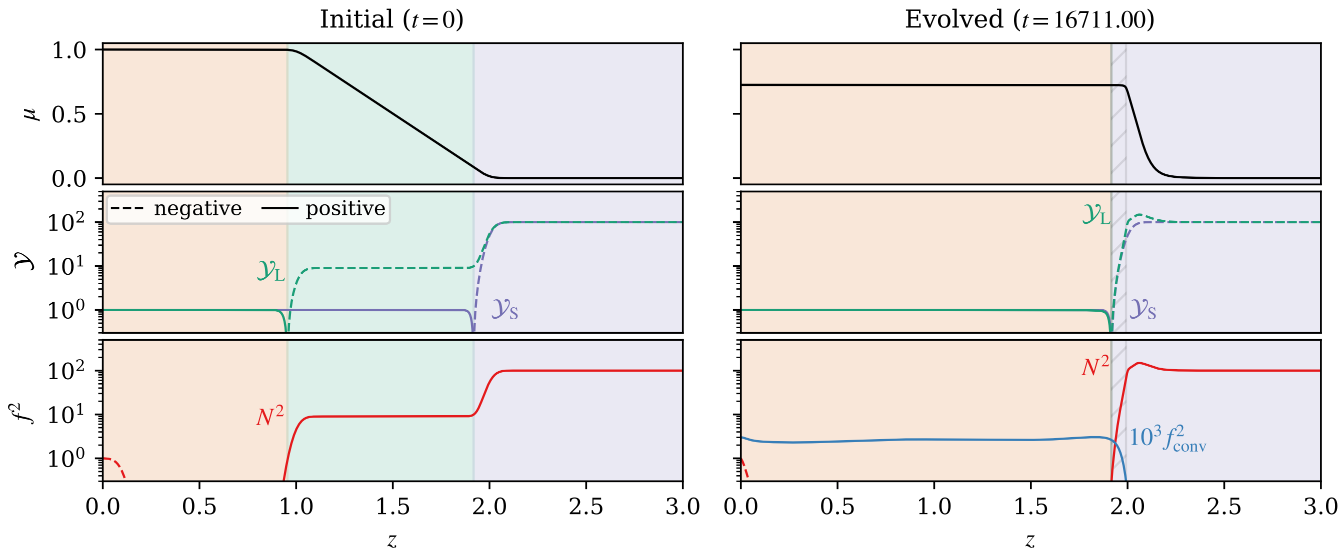

Figure 2. Horizontally-averaged profiles are shown for the composition (top), the discriminants $\mathcal{Y}_\mathrm{S}$ and $\mathcal{Y}_\mathrm{L}$ (middle, Eqns. 1 & 2), and the Brunt-Väisälä frequency $N^2 = -\mathcal{Y}_\mathrm{L}$ and the square convective frequency f^2_conv (bottom, Eqn. 3). Positive and negative values are respectively solid and dashed lines. We show the initial (left) and evolved (right, time-averaged over 100 convective overturn times) states. Note that there are no motions in the initial state, so $f^2_\mathrm{conv} = 0$ and does not appear. The background color is orange in CZs, green in SZs, and purple in RZs per Section 2. The lightly hashed background region in the evolved RZ is the mechanical overshoot zone.

"stiffness" of the radiative-convective interface,

$$\mathcal{S} = \frac{N^2|_\mathrm{RZ}}{f^2_\mathrm{conv}|_\mathrm{CZ}}, \tag{4}$$

which is related to the oft-studied Richardson number. Boundaries with a low stiffness $\mathcal{S} \lesssim 10$ easily deform in the presence of convective flows, but convective boundaries in stars often have $\mathcal{S} \gtrsim 10^6$. Note that the time to entrain the SZ scales like $\mathcal{S}^\alpha \tau_\mathrm{dyn}$, where α is an $\mathcal{O}(1)$ positive exponent and τ_dyn is the dynamical timescale (Turner 1968; Fuentes & Cumming 2020). Due to this $\mathcal{S}$ dependence, we study a large value of $\mathcal{S} \sim 10^4$ in the statistically-stationary state to ensure our simulations are in the right regime to study entrainment at a stellar convective boundary. Since the relevant timescale of evolution on the main sequence is the nuclear time τ_nuc, and since $\tau_\mathrm{nuc}/\tau_\mathrm{dyn} \gg \mathcal{S}^\alpha$ even for $\mathcal{S} \sim 10^6$, we expect CZs to entrain SZs during a single stellar evolution time step.

Finally, Figure 3 displays a Kippenhahn-like diagram of the simulation's height vs. time to show evolutionary trends. The roots of $\mathcal{Y}_\mathrm{L}$ and $\mathcal{Y}_\mathrm{S}$ are respectively shown as orange (Ledoux boundary) and purple (Schwarzschild boundary) lines. The CZ is colored orange and sits below the Ledoux boundary, the RZ is colored purple and sits above the Schwarzschild boundary, and the SZ is colored green and is between these boundaries. Convection motions overshoot above the Ledoux boundary. The height where the horizontally-averaged kinetic energy falls below 10% of its bulk-CZ value is marked with a black line, and the hashed region below it is the overshoot zone. We note that the black line and overshoot zone roughly correspond with the maximum of $\partial\mu/\partial z$ (Fig. 2, upper right), so this describes overshoot well. Importantly, note that the Schwarzschild and Ledoux boundaries start at different heights, but 3D convective mixing causes them to converge on dynamical timescales.

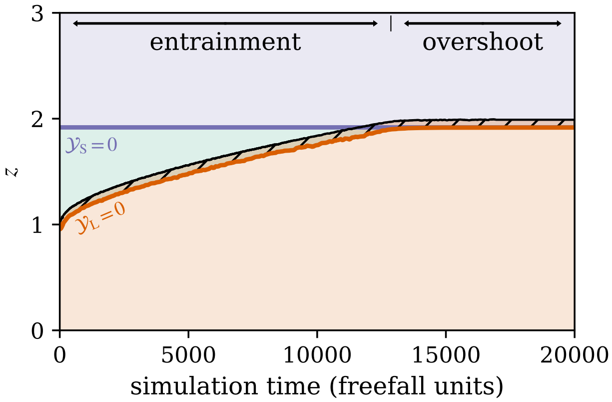

Figure 3. A Kippenhahn-like diagram of the simulation evolution. The y-axis is simulation height and the x-axis is simulation time. The orange line denotes the Ledoux boundary ($\mathcal{Y}_{\rm L} = 0$); the CZ is below this and is colored orange. The purple line denotes the Schwarzschild boundary ($\mathcal{Y}_{\rm S} = 0$); the RZ is above this and is colored purple. The semiconvective region between these boundaries is colored green. The overshoot zone is hashed, and the black line denotes the top of this region. The simulation has an "entrainment phase" while the CZ expands, and a pure "overshoot phase" where the convective boundary does not advance. Note: The simulation has only evolved to $t = 17000$, and I extended the end of this; it is running to 20000.

4. CONCLUSIONS & DISCUSSION

In this letter, we presented a 3D simulation of a convection zone and its boundary. The convective boundary was initially compositionally stable but weakly thermally unstable (Ledoux stable but Schwarzschild unstable). Entrainment caused the convective boundary to advance until the boundary was stable by both the Schwarzschild and Ledoux criteria.

This simulation demonstrates that the Ledoux criterion *instantaneously* describes the location of a convective boundary. However, when the dynamical convective overturn timescale is short compared to the evolutionary timescale $t_{\rm evol} \gg \mathcal{S}^{\alpha} t_{\rm dyn}$ (see Sec. 3), the statistically-stationary location of the convective boundary will coincide with the Schwarzschild boundary. These 3D dynamics support the claim that "logically consistent" implementations of mixing length theory (Gabriel et al. 2014; Paxton et al. 2018, 2019) should have convective boundaries which are Schwarzschild-stable. Modern algorithms like the MESA software instrument's "convective pre-mixing" (CPM, Paxton et al. 2019) should agree with our results. The results of 1D stellar evolution calculations should not depend on the choice of stability criterion used when $t_{\rm evol} \gg \mathcal{S}^{\alpha} t_{\rm dyn}$.

We note briefly that many SZs (the middle layer of our simulations) in stars are unstable to oscillatory double-diffusive convection (ODDC). ODDC mixes composition gradients even more rapidly than the entrainment studied here, and has been studied extensively in local simulations (Mirouh et al. 2012; Wood et al. 2013; Xie et al. 2017); see the review of Garaud (2018). Moore & Garaud (2016) apply ODDC to the regions outside core convection zones in main sequence stars, and their results suggest that ODDC formulations should be widely included in stellar models.

For stages in stellar evolution where $\mathcal{S}^{\alpha} t_{\rm dyn} \sim t_{\rm evol}$, implementations of time-dependent convection (TDC, Kuhfuss 1986) should be employed to properly capture convective dynamics and the advancement of convective boundaries. The advancement of convective boundaries by e.g., entrainment in TDC implementations should be informed by time-dependent theories and simulations (e.g., Turner 1968; Fuentes & Cumming 2020).

The purpose of this study was to understand how the Ledoux boundary location evolves over time, and whether it coincides with the Schwarzschild boundary at late times. A detailed examination of convective overshoot is beyond the scope of this work (but see e.g., Korre et al. 2019). We furthermore constructed the simulations in this work to have negligible convective penetration per Anders et al. (2021). Finally, in stars, $\nabla_{\rm rad}$ and the Schwarzschild boundary location depend upon μ, but we made the assumption that the radiative conductivity and $\nabla_{\rm rad}$ do not depend on μ for simplicity. The nonlinear feedback between these effects should be studied in future work, but we do not expect that the fundamental takeaways of this work should change.

In summary, we find that the Ledoux criterion provides the instantaneous location of the convective boundary, and the Schwarzschild criterion provides the location of the convective boundary in a statistically stationary state; in this final state, the Ledoux and Schwarzschild criteria agree.

We thank Meridith Joyce, Anne Thoul, Dominic Bowman, Jared Goldberg, Tim Cunningham, Falk Herwig, Kyle Augustson, (OTHERS?) for useful discussions which helped improve our understanding. EHA is funded as a CIERA Postdoctoral fellow and would like to thank CIERA and Northwestern University. AEF acknowledges support from NSF Grant Nos. AST-1814327 and AST-1908338. This research was supported in part by the National Science Foundation under Grant No. PHY-1748958, and we acknowledge the hospitality of KITP during the Probes of Transport in Stars Program. Computations were conducted with support from the NASA High End Computing (HEC) Program through the NASA Advanced Supercomputing (NAS) Division at Ames Research Center on Pleiades with allocation GID s2276. The Flatiron Institute is supported by the Simons Foundation.

APPENDIX

A. MODEL & INITIAL CONDITIONS

In this work we study the simplest possible system: incompressible, Boussinesq convection with a composition field. These equations are

$$\boldsymbol{\nabla}\cdot\boldsymbol{u} = 0 \tag{A1}$$

$$\partial_t \boldsymbol{u} + \boldsymbol{u}\cdot\boldsymbol{\nabla}\boldsymbol{u} + \boldsymbol{\nabla}\varpi = \left(T - \frac{\mu}{\mathrm{R}_0}\right)\hat{z} + \frac{\mathrm{Pr}}{\mathrm{Pe}}\boldsymbol{\nabla}^2\boldsymbol{u}, \tag{A2}$$

$$\partial_t T + \boldsymbol{u}\cdot(\boldsymbol{\nabla}T - \hat{z}\,\partial_z T_{\rm ad}) + \boldsymbol{\nabla}\cdot[-\kappa_{T,0}\boldsymbol{\nabla}\overline{T}] = \frac{1}{\mathrm{Pe}}\boldsymbol{\nabla}^2 T', \tag{A3}$$

$$\partial_t \mu + \boldsymbol{u}\cdot\boldsymbol{\nabla}\mu = \frac{\tau_0}{\mathrm{Pe}}\boldsymbol{\nabla}^2\overline{\mu} + \frac{\tau}{\mathrm{Pe}}\boldsymbol{\nabla}^2\mu'. \tag{A4}$$

Here, $\boldsymbol{u}$ is velocity, T is temperature, and μ is concentration. Bars (e.g., $\overline{T}$) represent the horizontally-averaged component of a field and primes (e.g., T') denote all fluctuations around that background. The adiabatic temperature gradient is $\partial_z T_{\rm ad}$ and the nondimensional control parameters are

$$\mathrm{Pe} = \frac{\mathrm{u_{ff}}\ell_{\rm conv}}{\kappa_{\rm T}}, \qquad \mathrm{R}_0 = \frac{|\alpha|\Delta\mathrm{T}}{|\beta|\Delta\mu}, \qquad \mathrm{Pr} = \frac{\nu}{\kappa_T}, \qquad \tau = \frac{\kappa_\mu}{\kappa_T}, \tag{A5}$$

where the nondimensional freefall velocity is $\boldsymbol{u}_{\rm ff} = \sqrt{|\alpha| g \ell_{\rm conv}\Delta T}$ (with gravitational acceleration g), $\ell_{\rm conv}$ is the initial depth of the convection zone, $\Delta\mu$ is the composition change across the Ledoux stable region, $\Delta T = \ell_{\rm conv}(\partial_z T_{\rm rad} - \partial_z T_{\rm ad})$ is the superadiabatic temperature scale of the convection zone, α and β are the coefficients of expansion for T and μ, ν is the viscosity, κ_T is the thermal diffusivity, and κ_μ is the compositional diffusivity. Eqns. A1-A4 are identical to Eqns. 2-5 in Garaud (2018), except we modify the diffusion coefficients acting on $\overline{T}$ ($\kappa_{T,0}$) and $\overline{\mu}$ (τ_0). By doing this, the radiative temperature gradient $\partial_z T_{\rm rad} = -\mathrm{Flux}/\kappa_{\rm T,0}$ can change with height, and we reduce diffusion on $\overline{\mu}$ to ensure its evolution is due to advection.

We define the Ledoux and Schwarzschild discriminants

$$\mathcal{Y}_{\rm S} = \left(\frac{\partial T}{\partial z}\right)_{\rm rad} - \left(\frac{\partial T}{\partial z}\right)_{\rm ad}, \quad \mathcal{Y}_{\rm L} = \mathcal{Y}_{\rm S} - \mathrm{R}_0^{-1}\frac{\partial\mu}{\partial z}, \tag{A6}$$

and in this nondimensional system the Brunt-Väisälä frequency is the negative of the Ledoux discriminant $N^2 = -\mathcal{Y}_{\rm L}$.

In this work, we study a three-layer model in $z = [0, 3]$,

$$\left(\frac{\partial T}{\partial z}\right)_{\rm rad} = \left(\frac{\partial T}{\partial z}\right)_{\rm ad} + \begin{cases} -1 & z \leq 2 \\ 10\mathrm{R}_0^{-1} & z > 2 \end{cases}, \tag{A7}$$

$$\frac{\partial \mu_0}{\partial z} = \begin{cases} 0 & z \leq 1 \\ -1 & 1 < z \leq 2 \\ 0 & 2 < z \end{cases}, \tag{A8}$$

We set $\mu = 1$ at $z = 0$ and $T = 1$ at $z = 3$. The the intial temperature profile has $\partial_z T_0 = \partial_z T_{\rm rad}$ everywhere except between $z = [0.1, 1]$ where $\partial_z T_0 = \partial_z T_{\rm ad}$. We set $(\partial T/\partial z)_{\rm ad} = -1 - 10\mathrm{R}_0^{-1}$.

B. SIMULATION DETAILS & DATA AVAILABILITY

We time-evolve equations A1-A4 using the Dedalus pseudospectral solver (Burns et al. 2020, git commit 1339061) using timestepper SBDF2 (Wang & Ruuth 2008) and safety factor 0.3. All variables are spectral expansions of Chebyshev coefficients in the vertical (z) direction ($n_z = 512$ between $z = [0, 2.25]$ plus $n_z = 64$ between $z = [2.25, 3]$) and as $(n_x,\ n_y) = (192,\ 192)$ Fourier coefficients in the horizontally periodic (x, y) directions. Our domain spans $x \in [0, L_x]$, $y \in [0, L_y]$, and $z \in [0, L_z]$ with $L_x = L_y = 4$ and $L_z = 3$. To avoid aliasing errors, we use the 3/2-dealiasing rule in all directions. To start our simulations, we add random noise temperature perturbations with a magnitude of 10^{-6} to the initial temperature profile.

Spectral methods with finite coefficient expansions cannot capture true discontinuities. To approximate discontinuous functions such as Eqns. A7 & A8, we define a smooth Heaviside step function centered at $z = z_0$,

$$H(z; z_0, d_w) = \frac{1}{2}\left(1 + \mathrm{erf}\left[\frac{z - z_0}{d_w}\right]\right). \tag{B9}$$

where erf is the error function and we set $d_w = 0.05$. The simulation in this work uses $\mathcal{P} = 3.2 \times 10^3$, $\mathrm{R}_0^{-1} = 10$, $\mathrm{Pr} = \tau = 0.5$, $\tau_0 = 1.5 \times 10^{-3}$, and $\kappa_{T,0} = \mathcal{P}^{-1}[(\partial T/\partial z)_{\mathrm{rad}}|_{z=0}]/(\partial T/\partial z)_{\mathrm{rad}}$

We produce figures 2 and 3 using matplotlib (Hunter 2007; Caswell et al. 2021). We produce figure 1 using plotly (Inc. 2015) and matplotlib. All of the Python scripts used to run the simulations in this paper and to create the figures in this paper are publicly available in a git repository (https://github.com/evanhanders/schwarzschild_or_ledoux) and in a Zenodo repository (?).

REFERENCES

Anders, E. H., Jermyn, A. S., Lecoanet, D., & Brown, B. P. 2021, arXiv e-prints, arXiv:2110.11356. https://arxiv.org/abs/2110.11356

Andrassy, R., Herwig, F., Woodward, P., & Ritter, C. 2020, MNRAS, 491, 972, doi: 10.1093/mnras/stz2952

Andrassy, R., Higl, J., Mao, H., et al. 2021, arXiv e-prints, arXiv:2111.01165. https://arxiv.org/abs/2111.01165

Basu, S. 2016, Living Reviews in Solar Physics, 13, 2, doi: 10.1007/s41116-016-0003-4

Basu, S., Verner, G. A., Chaplin, W. J., & Elsworth, Y. 2012, ApJ, 746, 76, doi: 10.1088/0004-637X/746/1/76

Burns, K. J., Vasil, G. M., Oishi, J. S., Lecoanet, D., & Brown, B. P. 2020, Physical Review Research, 2, 023068, doi: 10.1103/PhysRevResearch.2.023068

Carlos, M., Meléndez, J., Spina, L., et al. 2019, MNRAS, 485, 4052, doi: 10.1093/mnras/stz681

Caswell, T. A., Droettboom, M., Lee, A., et al. 2021, matplotlib/matplotlib: REL: v3.3.4, v3.3.4, Zenodo, doi: 10.5281/zenodo.4475376

Claret, A., & Torres, G. 2018, ApJ, 859, 100, doi: 10.3847/1538-4357/aabd35

Cristini, A., Hirschi, R., Meakin, C., et al. 2019, MNRAS, 484, 4645, doi: 10.1093/mnras/stz312

Dumont, T., Palacios, A., Charbonnel, C., et al. 2021, A&A, 646, A48, doi: 10.1051/0004-6361/202039515

Farmer, R., Renzo, M., de Mink, S. E., Marchant, P., & Justham, S. 2019, ApJ, 887, 53, doi: 10.3847/1538-4357/ab518b

Fuentes, J. R., & Cumming, A. 2020, Physical Review Fluids, 5, 124501, doi: 10.1103/PhysRevFluids.5.124501

Gabriel, M., Noels, A., Montalbán, J., & Miglio, A. 2014, A&A, 569, A63, doi: 10.1051/0004-6361/201423442

Garaud, P. 2018, Annual Review of Fluid Mechanics, 50, 275, doi: 10.1146/annurev-fluid-122316-045234

Georgy, C., Saio, H., & Meynet, G. 2021, A&A, 650, A128, doi: 10.1051/0004-6361/202040105

Hunter, J. D. 2007, Computing in Science and Engineering, 9, 90, doi: 10.1109/MCSE.2007.55

Inc., P. T. 2015, Collaborative data science, Montreal, QC: Plotly Technologies Inc. https://plot.ly

Johnston, C. 2021, A&A, 655, A29, doi: 10.1051/0004-6361/202141080

Jones, S., Andrassy, R., Sandalski, S., et al. 2017, MNRAS, 465, 2991, doi: 10.1093/mnras/stw2783

Kaiser, E. A., Hirschi, R., Arnett, W. D., et al. 2020, MNRAS, 496, 1967, doi: 10.1093/mnras/staa1595

Korre, L., Garaud, P., & Brummell, N. H. 2019, MNRAS, 484, 1220, doi: 10.1093/mnras/stz047

Kuhfuss, R. 1986, A&A, 160, 116

Meakin, C. A., & Arnett, D. 2007, ApJ, 667, 448, doi: 10.1086/520318

Mehta, A. K., Buonanno, A., Gair, J., et al. 2022, ApJ, 924, 39, doi: 10.3847/1538-4357/ac3130

Mirouh, G. M., Garaud, P., Stellmach, S., Traxler, A. L., & Wood, T. S. 2012, ApJ, 750, 61, doi: 10.1088/0004-637X/750/1/61

Moore, K., & Garaud, P. 2016, ApJ, 817, 54, doi: 10.3847/0004-637X/817/1/54

Morrell, S. A. F. 2020, PhD thesis, University of Exeter

Paxton, B., Schwab, J., Bauer, E. B., et al. 2018, ApJS, 234, 34, doi: 10.3847/1538-4365/aaa5a8

Paxton, B., Smolec, R., Schwab, J., et al. 2019, ApJS, 243, 10, doi: 10.3847/1538-4365/ab2241

Pedersen, M. G., Aerts, C., Pápics, P. I., et al. 2021, arXiv e-prints, arXiv:2105.04533. https://arxiv.org/abs/2105.04533

Pinsonneault, M. 1997, ARA&A, 35, 557, doi: 10.1146/annurev.astro.35.1.557

Salaris, M., & Cassisi, S. 2017, Royal Society Open Science, 4, 170192, doi: 10.1098/rsos.170192

Scott, L. J. A., Hirschi, R., Georgy, C., et al. 2021, MNRAS, 503, 4208, doi: 10.1093/mnras/stab752

Sestito, P., & Randich, S. 2005, A&A, 442, 615, doi: 10.1051/0004-6361:20053482

Staritsin, E. I. 2013, Astronomy Reports, 57, 380, doi: 10.1134/S1063772913050089

Turner, J. S. 1968, Journal of Fluid Mechanics, 33, 183, doi: 10.1017/S0022112068002442

Viani, L. S., & Basu, S. 2020, ApJ, 904, 22, doi: 10.3847/1538-4357/abba17

Wang, D., & Ruuth, S. J. 2008, Journal of Computational Mathematics, 26, 838. http://www.jstor.org/stable/43693484

Wood, T. S., Garaud, P., & Stellmach, S. 2013, ApJ, 768, 157, doi: 10.1088/0004-637X/768/2/157

Woodward, P. R., Herwig, F., & Lin, P.-H. 2015, ApJ, 798, 49, doi: 10.1088/0004-637X/798/1/49

Xie, J.-H., Miquel, B., Julien, K., & Knobloch, E. 2017, Fluids, 2, doi: 10.3390/fluids2010006